Solar Energy 220 (2021) 217–229

Contents lists available at ScienceDirect

Solar Energy

journal homepage: www.elsevier.com/locate/solener

Dispatchable solar power using molten salt directly irradiated from above

Nicolas Calvet [a,*], Alexander H. Slocum [b], Antoni Gil [a,b], Benjamin Grange [a,1], Radia Lahlou [a], Tyler T. Hamer [b], Miguel Diago [a,2], Melanie Tetreault-Friend [c,3], Daniel S. Codd [d], David L. Trumper [b], Peter R. Armstrong [a]

[a] Department of Mechanical Engineering, Masdar Institute, Khalifa University of Science and Technology, Masdar Institute Solar Platform, PO Box 127788, Abu Dhabi, United Arab Emirates
[b] Department of Mechanical Engineering, Massachusetts Institute of Technology, 77 Massachusetts Ave, Cambridge, MA 02139, United States
[c] Department of Nuclear Science and Engineering, Massachusetts Institute of Technology, 77 Massachusetts Ave, Cambridge, MA 02139, United States
[d] Shiley-Marcos School of Engineering, University of San Diego, 5998 Alcala Park, San Diego, CA 92110, United States

ARTICLE INFO

Keywords:
Concentrated solar power (CSP)
Thermal energy storage (TES)
Molten salt
Direct absorption receiver (DAR)
Volumetric solar receiver
Beam down tower
Secondary concentrator

ABSTRACT

Concentrating solar power (CSP) with thermal energy storage (TES) presents the major advantage over solar photovoltaics of *dispatchability*. High thermodynamic efficiencies achieved by collecting and storing heat at higher temperatures, and recent maturing of the technology, are making molten-salt central receiver plants the preferred option for CSP. To explore potential further improvements in CSP efficiency and cost the world's first direct absorption molten salt volumetric receiver/storage system was built at pilot scale, commissioned and monitored. In this demonstration a 100 kW_{th} beam-down tower directs solar radiation through a final concentrator into the open aperture of a 1.94 m high and 1.25 m internal diameter tank receiver situated near the ground. The receiver tank is filled with 3,800 kg of 60–40 wt% $NaNO_3$-KNO_3 and serves as a stratified or mixed single tank thermal store that can satisfy evening peak loads or provide baseload power through the night. Compared to the parasitic loads of a conventional tower-receiver plant, the energy needed for salt transport from receiver to TES and morning preheat is negligible for this new system. The hot-spot problem of tubular receivers is eliminated and. the combined receiver/storage tank reduces component costs. In-situ initial melting was accomplished using solar energy as the primary input. Thermal stratification was maintained by daily cycling of a divider plate and occasional mixing plate actions and hot spots were never observed during several months' operation between 250 and 500 °C. Three cycles of complete salt freezing and in-situ on-sun re-melting were tested with no operational difficulty and no discernible damage.

1. Introduction

1.1. Background

At the end of 2019 an inventory of the world's operational concentrated solar power (CSP) capacity stood at about 6.451 GW, a 20% increase from the 5.133 GW reported at the end of 2017 (SolarPACES, 2020). Although far behind global photovoltaic capacity of 580 GW, and wind power capacity of 622 GW, CSP is the only technology of the three that can economically provide dispatchable power at large scale. Dispatchability is made possible by highly cost-effective thermal energy storage (TES). In addition, the cost of CSP has been dropping steadily in recent years as industry climbs the learning curve (Pitz-Paal, 2017; Lilliestam et al., 2017), consistent with the United States Department of Energy (DOE) SunShot Initiative targets (USDOE, 2017). This Initiative aims for levelized costs of electricity (LCOE) to reach $0.10 and $0.05 per kilowatt-hour for CSP peaker (≤6h storage) and CSP baseload (≥12 h storage) plants, respectively, by 2030. Growth of CSP has been rapid in the recent decade (Lilliestam et al., 2017), initially due to pioneers in USA and Spain, then to markets emerging in the Middle East and North and South Africa, and recently to entry of China and Chile. DOE cost objectives have been met by some commercial plants in regions of high

* Corresponding author at: Chair of the Masdar Institute Solar Platform, Department of Mechanical Engineering, Masdar Institute, United Arab Emirates.
E-mail address: nicolas.calvet@ku.ac.ae (N. Calvet).
[1] Present address: PROMES-CNRS Laboratory, 7 rue du Four Solaire, 66120 Font-Romeu-Odeillo-Via, France.
[2] Present address: Institut de recherche d'Hydro-Québec (IREQ), 1800 boul. Lionel-Boulet, Varennes, Québec J3X 1S1, Canada.
[3] Present address: Department of Mechanical Engineering, McGill University, 817 Sherbrooke Street West, Montreal, QC H3A 0C3, Canada.

https://doi.org/10.1016/j.solener.2021.02.058
Received 31 July 2020; Received in revised form 17 February 2021; Accepted 24 February 2021
Available online 1 April 2021

direct normal irradiance (DNI) like Chile (SolarReserve with LCOE less than 0.05 $/kWh, November 2017). Continuing efforts to develop and adopt innovative technologies will undoubtedly further reduce cost and improve efficiency.

The current state of the art in high-temperature TES is a two-tank molten salt technology in which liquid salt stores energy as sensible heat at atmospheric pressure. In the case of parabolic trough (indirect TES) systems, salt is pumped from the relatively cold tank (290 °C) through an oil-to-salt heat exchanger where it is heated to 384 °C by synthetic oil returning hot from the solar field. To discharge TES, the salt is pumped back through the salt-to-oil heat exchanger, and stored in the cold tank. This charge–discharge cycle is repeated daily.

The first commercial molten-salt TES plant came on line in 2008 with the ANDASOL 1 parabolic trough plant of 50 MW_e in Granada Spain, where 28,500 tonnes of nitrate salts are stored in two tanks of 14 m height providing a storage capacity of 7.5 h at full power. The Solana parabolic trough CSP plant (SolarPACES, 2020) in Arizona, which reached full capacity in 2015, has a 6-hour TES provided by 125,000 tonnes of molten salt.

Motivated by the quest for higher temperatures (Baum et al., 1957; Hildebrandt and Vant-Hull, 1975), some early designs (Skinrood et al., 1974), as well as the most recent (Solar Two and Solar Tres) and planned central receiver plants (SolarPACES, 2020) are designed to pump molten salt directly from a cold tank to a tower receiver where it is heated to 565 °C. To discharge, the salt is pumped from the hot tank through heat exchangers that produce superheated steam for a turbine. Tubular molten salt receivers were originally tested in the 1980′s by Sandia (USA) in the Molten Salt Electricity Experiment (Delameter and Bergan, 1986) and by EDF in France with the THEMIS power tower demonstration plant of 2.5 MW_e (Drouot and Hillairet, 1984) using a ternary nitrate/nitrite eutectic mixture of KNO_3, $NaNO_2$, and $NaNO_3$ (53%, 40%, and 7% by mass). Later another demonstration was developed in the Mojave Desert (California, USA) in the 90′s where Solar ONE was modified into Solar TWO using a similar two-tank system (Speidel et al., 1999) filled with a different eutectic mixture of $NaNO_3$, KNO_3 (60%, 40%).

The receiver is generally considered to be the most critical and highly stressed part of a central receiver plant (Mark Mehos et al., 2020) and has been the object of research and innovation for decades (Ho, 2017). A variety of concepts have reached high temperature testing in laboratories (Ho and Iverson, 2014). The first commercial molten salt power tower, Gemasolar (19.9 MW_e) was built by Torresol (Masdar/Sener Joint Venture) in Seville Spain to generate electricity 24/7.

While now considered a proven technology, molten salt TES still presents certain limitations such as low capture efficiency of external tubular receivers, high parasitic costs associated with operation of pumps and heat tracing, and long-term durability concerns (Reilly and Kolb, 2001; Ho and Iverson, 2014).

Some of the limitations (as well as advantages) of molten salt are linked to its intrinsic properties. The first constraint is its relatively high freezing temperature. A 60/40 nitrate salt mixture starts to melt at 220 °C when heated and starts to crystalize around 230 °C (AlQaydi et al., 2016) when cooled. Electric heat tracing used to preheat the pipes and to prevent salt freezing in molten salt central receiver plants results in significant parasitic energy consumption. The most preheat-energy consuming component of a tower receiver plant is the receiver itself where the large exposed surface area of salt-carrying panel headers and tubes loses heat during the entire preheat process. For a big receiver (600 MW_{th}) around 1 MW_e is needed to raise the temperature of the headers to 280 °C in less than 2 h. Even with solar preheating of the exposed receiver panels, all manifolds, headers, piping and valves between the receiver and TES tanks must be fully heat-traced. Daily preheating of the receiver and other nocturnally drained piping in a 100 MW_e plant consumes around 1.5 MWh_e in parasitic energy. Total consumption of all the freeze protection and preheat devices may approach 1% of a plant's average electrical output.

In addition to ongoing costs of parasitic energy consumption, the installation costs of heat tracing in a commercial plant are substantial due to the large heating capacity needed to compensate heat losses, preheat fast and, in worst case, thaw frozen salts. Meticulous installation of tracing is critical to reliable operation (Mark Mehos et al., 2020). In a 100 MW_e commercial plant, the total heat tracing capacity can be above 7 MW_e (G. Vazquez, 2017).

A comparable or even larger factor contributing to operating costs of a utility-scale power tower is the parasitic consumption related to pumping cold salt up the tower which constitutes 4 to 7% of annual plant production for large plants (>100 MW_e) designed for 24/7 production, and up to 10% for smaller plants (~20 MW_e) (Vazquez, 2017), (Anonymous, 2018).

Further contributing to capital costs are the several kilometres of steel tubes and numerous connections, valves and pumps. Other cost and performance factors pertain to system design, especially the simple fact that molten salt is contained in steel tubes in the receiver. Thermal cycling under partly cloudy conditions produces thermal stress in steel parts of the solar receiver; transient thermal strains (Ho and Iverson, 2014), potentially coupled with salt blockages, may cause the receiver tubes to rupture leading to salt leakage, down time, and expensive repairs.

Because the receiver itself is a significant cost and performance pinch point, various direct absorption receivers (DAR) have been proposed (West, 1987; Viskanta, 1987; Bohn and Green, 1989; Epstein et al., 1999; Singer et al., 2013), in which the solar flux is focused directly into a flowing heat transfer medium rather than onto the outer surface of a containing vessel or channel e.g. receiver tubes. In contrast to conventional closed-channel absorbers, the problems of hot spots and cyclic thermal stresses are largely eliminated by a DAR. West proposed an elliptic shape DAR, over which liquid molten salt would flow as a thin film down the surface of a tilted plate located at the top of a power tower, using a eutectic mixture of sodium-, potassium-, and lithium-carbonates that is a stable liquid between 397 °C and 900 °C (West, 1987). A molten nitrate-salt film absorber was operated under a 600 kW/m^2 solar simulator (Bohn and Green, 1989). However, stability and uniformity of large-scale molten salt falling films have yet to be fully demonstrated (Ho and Iverson, 2014). Other DAR concepts have employed directly irradiated particle streams (Iniesta et al., 2015). In contrast to the liquid DARs, particle-stream DAR schemes face problems of erosion on receiver and heat exchanger surfaces, of heat-exchanger thermal performance, and of complex and inefficient particle-tower lifting systems. The status and challenges for progress in high temperature receivers have been summarized in (Ho, 2017).

A novel molten-salt DAR concept that uses volumetric rather that falling film absorption by combining receiver and storage in a ground level tank has been proposed and developed at lab scale (Slocum et al., 2011). Although distinctive in form from previous DAR, volumetric (VAR) and cavity receiver concepts, the new receiver possess the efficient solar-to-heat conversion properties of all three:

- DAR: incident radiation is directly absorbed by the heat transfer fluid; the heat transfer resistance of a tubular receiver and the cost and optical losses of a window are avoided.
- VAR: the absorption coefficient of molten salt in most of the terrestrial solar spectrum is low but not zero: >50% broadband attenuation takes place over a ~ half meter path.
- Cavity Receiver: a cavity receiver can achieve higher optical efficiency and lower aperture thermal losses than a comparable external receiver.

Combining the receiver and TES in a single tank reduces component costs and largely eliminates transport and trace-heating costs. Replacing receiver tubes by an unpressurized open tank greatly reduces the magnitude of expansion/contraction stress cycles induced by thermal transients. In recognition of conceptual similarity (notwithstanding the

vast difference in collection temperature enabled by concentrating optics) to the salt-gradient solar pond (Tabor, 1981) the new receiver/TES concept was dubbed CSPonD: Concentrating Solar Power on Demand. A laboratory-scale demonstration using 7 L of molten salt and a 10.5 kW solar simulator with flux >60 kW/m^2 (60 suns) was performed by Codd (2011) and the spectral absorption coefficient was characterized (Passerini, 2010).

1.2. CSPonD demonstration pilot

To extend independent efforts in their complementary areas of expertise Masdar Institute and MIT partnered to design, build, and operate a larger-scale prototype receiver suitable for on-sun testing at the pre-existing 100 kW$_{th}$ Masdar beam-down optical experiment (MBDOE) located at the Masdar Institute Solar Platform (Calvet et al., 2016) and shown in Fig. 1 (Hasuike et al., 2009; Mokhtar et al., 2014; Meyers, 2011; Kumar, 2015; Diago et al., 2018a,b; Diago et al., 2020). A three-year MI-MIT program was initiated in 2014 to complete the extensive efforts summarized below.

A combined receiver and TES tank was designed to be placed near the ground below the central reflector (CR) tower such that concentrated solar flux enters via an open aperture at the top of the tank and is directly absorbed in the volume of the semi-transparent molten salt or, to lesser extent, by interior surfaces of the hot region cavity (Fig. 2a). A loose-fitting insulated plate, which separates the upper hot salt from the lower relatively cold region, is actuated to move downwards while charging and upwards while discharging. During charging, cold fluid enters the upper hot region via the lateral annular gap in response to the plate's downward motion. A uniform hot-zone temperature is maintained throughout the heating process by means of a mixing plate. The hot fluid may be extracted 24/7 from the outlet at the top to pass through a steam generator (thermal load simulated by a thermosiphon salt-to-air heat exchanger in this case) and is returned to the bottom inlet at the cold temperature as the insulating plate rises.

The test system (Fig. 2b), comprises a tank containing 3.8 tonnes of molten salt (Grange et al., 2015; Gil et al., 2015; Gil et al., 2016) (Suppl. Note 2), a final optical element (FOE) positioned to increase flux density at the tank inlet (Kumar, 2015), a FOE thermal management system, FOE flux scanning systems at its entry and exit (Lahlou et al., 2016, Lahlou et al., 2018) (Suppl. Note 1), an insulated tank lid, a divider plate (DP) and mixing plate (MP) with associated actuators (Hamer et al., 2017a,b; Hamer, 2018) (Suppl. Note 2), 263 thermocouples to measure salt, tank wall, and FOE temperatures (Suppl. Note 3), and a thermosiphon heat exchanger. A rotating mast (Suppl. Note 4), and a moveable platform (Suppl. Note 4) carry the FOE and the insulated tank lid. Precise mast motions of 0.4 m vertically and 90° in rotation allow closure of the tank aperture at night and when low DNI results in net loss at the tank inlet aperture, by moving the FOE away and placing the lid over the aperture.

The objective of this work is to demonstrate technical viability of a directly-irradiated volumetric molten salt receiver with collocated single-tank TES under real on-sun conditions at meaningful scale. The evolution of temperatures during on-sun charging (Fig. 5) demonstrate that absorption of incident radiation by the molten salt is indeed largely a volumetric absorption process. Analysis of thermal decay at night provides an estimate of tank jacket loss model coefficient. Further analysis of mean temperature trajectory with the lid open and heliostats defocused gives an estimate of radiation loss coefficient in terms of effective aperture area. Both loss models are consistent with theory. Receiver thermal efficiency was measured under experimental conditions of DNI = 570 W/m^2 and T$_{surf}$ = 455 °C with the existing heliostat field providing C = 145 and also estimated for a built out field (C = 600) under design conditions of DNI = 900 W/m^2 and T$_{surf}$ = 550 °C.

2. Methods

2.1. Instrumentation and control

Temperatures are measured by type K special-limits-of-error thermocouples allocated as follows: 117 in molten-salt tank via nine vertical rods each with 13 junctions (Fig. 13b of Suppl. Note 2); 9 distributed on tank exterior surface and insulation; 6 in resistance heaters; 124 on six

Fig. 1. CSPonD Demonstration, deployed on the central axis of existing Masdar beam-down tower and heliostat field, during operation in June 2017 at the Masdar Institute Solar Platform (MISP). The 100 kW$_{th}$ beam-down system employs 33 heliostats that reflect sunlight upward to a tower-mounted central reflector (CR), which reflects concentrated light down onto an upward-facing final concentrator (Final Optical Element, FOE) and corresponding CSPonD receiver.

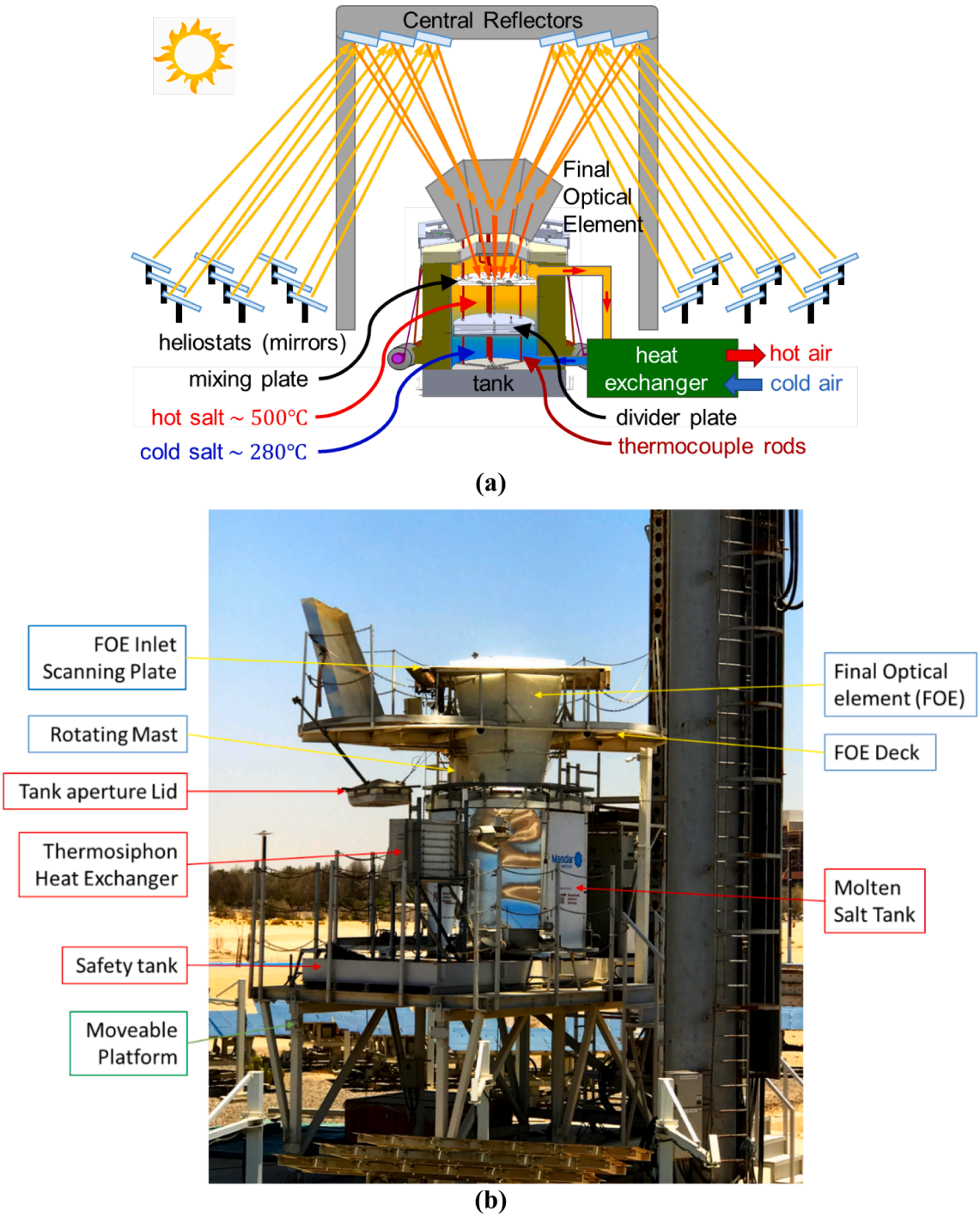

Fig. 2. (a) Schematic and (b) photo of the CSPonD demonstration with main elements labelled. A single tank holds both hot and cold salt, separated by a movable divider plate, thus serving as a receiver and TES tank simultaneously. An actuated plate is used to enhance mixing in the salt (mixing plate), and a final optical element (FOE) is positioned above the tank to increase solar flux at the tank aperture.

FOE facets (20 each plus 2 each on the flanges of facets 1 and 4—See Suppl. Note 1); 5 at heat exchanger salt- and air-side inlets and outlets. The thermocouple signals are sampled, converted from emf to temperature, and stored continuously every second.

Flux maps at the FOE inlet and outlet are generated by indirect measurement using CCD images of two near-Lambertian scanning targets each equipped with a 0.3-ms response heat flux sensor for calibrating the CCD intensity signals on each pixel map for conversion to flux map. Unfortunately, the flux sensors and corresponding amplifiers fell victim to the emirate's coastal desert environment preventing acquisition of flux maps during the molten salt tank experimental campaign. A flux map acquired before failure is compared to optical simulation results in Suppl. Note 1, section 5 along with its use to estimate receiver flux based on continuously measured DNI and heliostat cleanliness factors measured before each experiment.

Three hoists actuate the divider plate and three more actuate the mixing plate. Each hoist is driven by an electric winch whose cable passes through a single moving sheave block before returning to the hoist base to provide a 2:1 mechanical advantage. The moving block pulls a SS304 chain which passes over two idler sheaves on top of tank

before entering the molten salt (See Suppl. Note 2, sections 2 and 3). A hoist chain can only apply upward force on its plate. Each plate drops under its own weight while its winches unwind as the brakes disengage in small steps to avoid paying out slack cable.

The position of each hoist is controlled by a simple UP/DOWN/STAY control scheme and feedback from a string potentiometer connected to each moving sheave block. Plate positions are controlled within 1.0 cm.

2.2. Salt preparation and loading

Sodium nitrate and potassium nitrate salts were delivered in separate bags of about 1200 kg each (see Suppl. Note 5, Fig. S14). The granular salts, while stored outside for 12 months, had absorbed moisture and consolidated (aka caking or agglomeration) into large masses. Large blocks were first broken into small pieces using an electric impact hammer. The chunks of salt were then dumped onto a rubber mat divided into two piles of sodium nitrate and potassium nitrate salts. After further granulation by a vibratory compactor the salt was weighed and poured, alternating between $NaNO_3$ and KNO_3, into a holding box in the proper 60/40 mass ratio.

Before loading salt into the tank, the divider and mixing plates were positioned at the bottom to avoid overloading chains and winch spools by the dead weight of the still solid salt mass. Buckets of salt were poured directly into the tank through a chute placed between the raised FOE and the top of the tank collar as shown in Fig. 3a. Following this procedure (Fig. 3b) an initial salt mass of 1000 kg was loaded to commence an on-sun direct absorption salt melting process, previously unknown in the CSP industry, on the morning of June 5, 2017.

2.3. First melting

The beam-down concentrator was put into tracking mode on the day salt loading commenced, June 5, 2017, at 10:31 to heat the solid granular salt from ambient temperature to about 120 °C. Salt started to melt, as seen via a CCD camera looking downward from the tower, at a few points on the surface. Electric resistance heaters surrounding and under the floor of the tank were operated at 200 W to accelerate the heating process and avoid freezing the freshly melted salt that has percolated down from the top irradiated surface. At 5:30 pm, 850 kg more salt was added on top of the preheated salt and then the lid was closed at 5:53 pm. At the end of the first day with 1850 kg in the tank, temperatures of about 115 °C were observed and maintained overnight with help of the electric heaters. Fig. 4 shows the thermal evolution in the tank, as measured by a set of vertical thermocouple rods, during the five days of system start up.

During the second day, liquid salt pools grew progressively in depth from the top irradiated regions, and grew radially from the tank centerline where incident radiation is highest. As soon as a small melt pool formed, as recorded by the CCD camera, it would spread and chunks of solid salt could be seen falling from outside the irradiated region and sinking into the central pool of liquid. As the melt pool increased in size and salt beneath was heated by hot liquid entering it from above, water vapour and air entrained in the solid salt bubbled up to mix the salt phases even as the pool got deeper. This helped to rapidly melt the bulk salt towards the bottom of the tank. At the end of the second day 1150 kg granular salt was added on top of the 850 kg already melted following the same procedure as described for the first day.

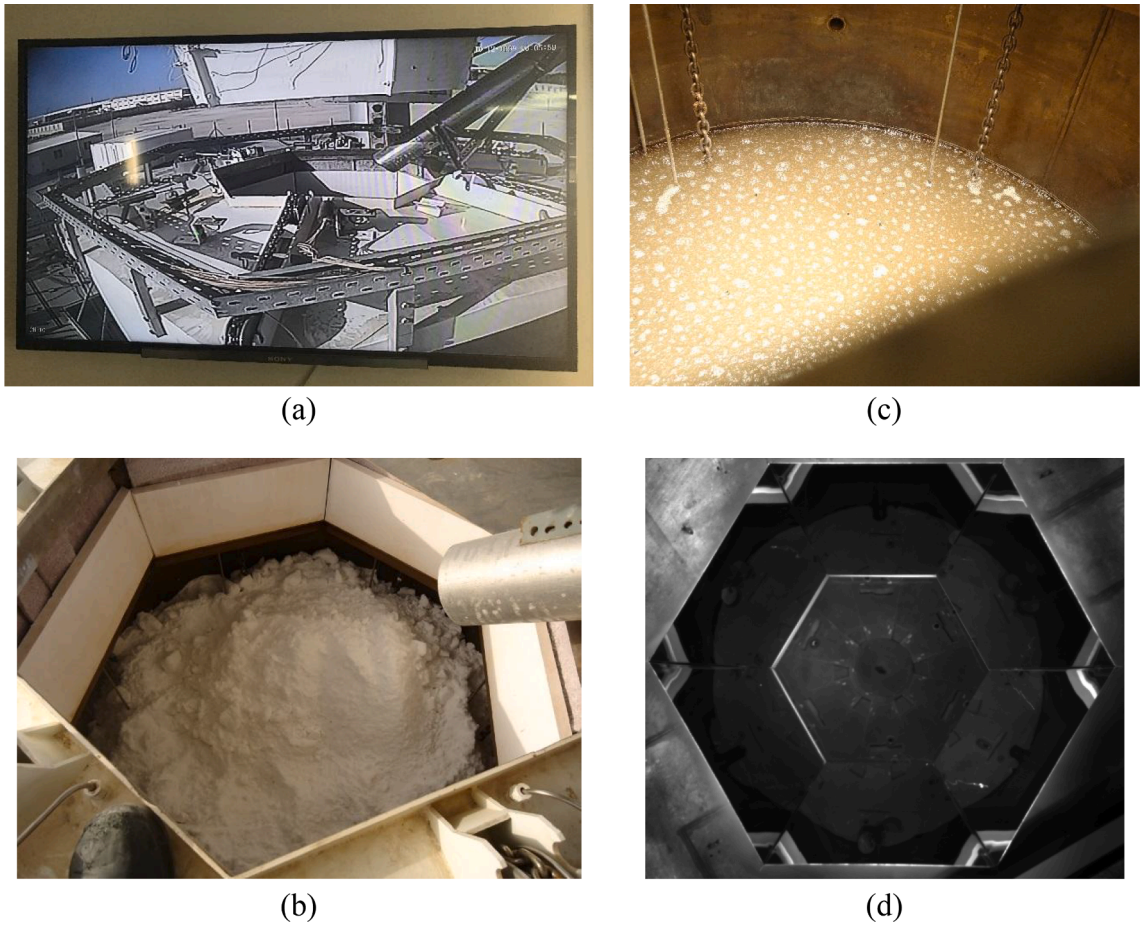

Fig. 3. (a) Safety monitoring screen showing the top of the tank and its aperture during loading of the salt using a chute; (b) Solid salt loaded into the tank via chute shown on the right, (c) Surface of the molten salt during the second day of melting, June 6, 2017 (vimeo.com/259461409) (d) Top view of the fully-melted salt from the tower reflector-mounted CCD camera after 4 days of non-operation, January 18,2018. MP is visible about 1 m below the molten salt surface.

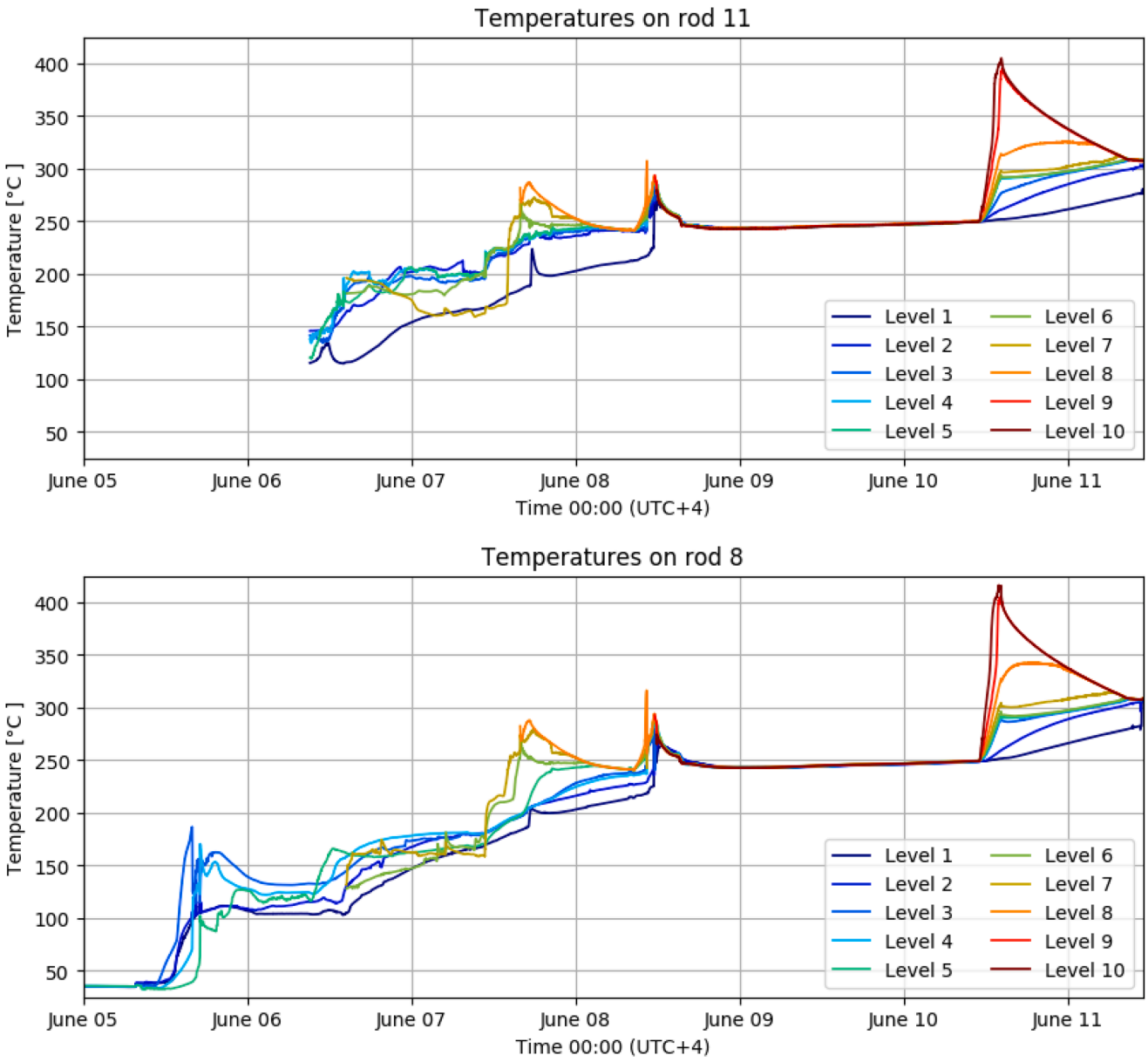

Fig. 4. Temperature evolution in the tank measured by two rods during the melting process starting on June 5, 2017. An upper-level temperature is plotted only after its source TC is reached by the rising salt level: Level 6 & 7 at 14:31 Jun-06; Level 8 at 15:56 Jun-07; Level 9 at 11:37 and Level 10 at 11:54 on Jun-08. Note that temperatures appear noisy up until Jun-08 because the salt is mainly in a granular state characterized by random movement (settling), very low bulk thermal diffusivity, and non-uniformity of temperature in horizontal as well as vertical directions. The liquid fraction becomes large enough (and continues to grow) on Jun-08 for temperatures to become uniform in the horizontal direction. From that day forward, stratified behaviour (expected with DP and MP fixed at their lowest positions) predominates when direct solar is available and focused into the tank, while thermal diffusion is sufficient for temperatures to equilibrate at night.

During the second night, the salt temperature equilibrated to around 200 °C.

On the third day, with 3000 kg of salt already in the tank, the evolution of bubbles resumed as the upper part was completely melted. An additional salt mass of 400 kg was added at the end of the third day. During the third night, the temperature was observed to equilibrate to 242.5 °C somewhat above the phase transition temperature. The salt was completely melted by the end of the fourth day as seen on Fig. 3c. Then 200 kg of salt were added and the system was not operated on the fifth day. Fig. 4 shows a plateau at 238 °C on the fourth night, gradually increasing through the fifth day to about 250 °C due to electric heat from the bottom of the tank. Finally, at the end of the sixth day, 200 kg were added to achieve the desired salt level, reaching a total of 3.8 tons of nitrate salt. In the next three months 27 experimental charging cycles and two freeze-melt cycles were monitored. The salt was then allowed to freeze and cool to ambient temperature for two months and was finally re-melted in January 2018. Fig. 3d shows the MP clearly visible under the molten salt on January 18. It is apparent that all impurities have settled to the bottom and the salt above is of very low turbidity and moderately high transparency.

Aside from the harsh summer working conditions (47 °C and humid), the melting process was straightforward. In contrast to the conventional molten salt start-up procedure, which requires an external fossil fuel fired melter, the salt was melted directly in the tank by solar radiation. In the four-day process approximately 80% of melting energy was solar heat from the beam down concentrator and the remaining 20% was from external electric tank heaters serving mainly to sustain tank temperature at night. These heaters are the same devices necessary in all salt TES tanks for standby heat during extended maintenance periods; they do not add to system parasitic energy in day-to-day plant operation.

2.4. Receiver performance evaluation

Receiver optical and thermal efficiencies are based on optical and thermal energy rates. We adopt the following definitions.

The solar radiation fluxes of interest are:

- $\dot{Q}_i$ total concentrated solar flux incident on the tank inlet aperture (W),
- $\dot{Q}_{reject}$ flux rejected by the receiver due to reflections at the salt surface or after interaction with interior surfaces (W), and
- $\dot{Q}_{abs}$ solar flux absorbed directly by the salt and, to a lesser extent, indirectly via the receiver's submerged inner surfaces (W), such that:

$$\dot{Q}_i = \dot{Q}_{abs} + \dot{Q}_{reject}. \tag{1}$$

The thermal fluxes of interest are:

- $\dot{Q}_{th-loss}$ the rate of total heat loss from the open tank (W), and
- $\dot{Q}_{stored}$ the net rate of heat stored in the salt (W), such that

$$\dot{Q}_{abs} = \dot{Q}_{stored} + \dot{Q}_{th-loss} \tag{2}$$

is the rate at which absorb solar radiation (1) is converted to heat when the aperture is open.

Note that total heat loss includes jacket as well as aperture losses by radiation and convection as identified in Supplementary Note N2.5. The solar (1) and thermal (2) energy balances are coupled by $\dot{Q}_{abs}$.

- *Receiver optical efficiency*

The receiver's optical efficiency is defined as:

$$\eta_{opt} = \frac{\dot{Q}_{abs}}{\dot{Q}_i} = 1 - \frac{\dot{Q}_{reject}}{\dot{Q}_i}. \tag{3}$$

A flux measurement system was designed to measure $\dot{Q}_i$ in-situ during receiver charging, (Suppl. Note 1, section 5). After a successful measurement of flux density contours at the the FOE inlet during preliminary water tank tests (results in Suppl. Note 1, section 5), the flux sensors and amplifiers were damaged. Flux at the receiver's inlet, $\dot{Q}_i$, could therefore not be measured during salt melting and subsequent daily on-sun charging.

Flux rejected at the salt surface by reflection, $\dot{Q}_{reject}$, was evaluated instead using the Fresnel equations embedded in a ray-tracing model of the entire optical system (Kumar, 2015). The ratio of reflected to incident flux depends on the angular distribution of rays incident on the salt surface (exiting the FOE) and therefore depends on sun position as well as the FOE geometry and the tower's central reflector (CR) canting angles. The receiver optical efficiency was therefore included in the objective function for FOE and CR geometry optimization (see Suppl. Note 1.1 and 1.3: Analysis of heliostat, CR and FOE optics).

- *Thermal efficiency*

Receiver thermal performance must be evaluated for two conditions:

1) Experimental conditions of DNI = 582 W/m^2 with sun near zenith, ambient temperature of 30 °C, salt surface temperature $T_{surface}$ = 434 °C, and existing (31 – of 33 – heliostat) fiels;
2) Commercial design point conditions of DNI = 900 W/m^2 with sun near zenith, ambient temperature of 40 °C, two cases of salt surface temperature $T_{surface}$ = 500 and 550 °C, and an extended heliostat field.

Performance at the commercial design point, while not directly measurable, can be confidently estimated using a field scale-up ratio and the receiver's optical efficiency and measured thermal loss models to give an idea of receiver efficiency one can expect to achieve in a utility-scale plant.

The receiver's thermal efficiency is defined as:

$$\eta_{th} = \frac{\dot{Q}_{stored}}{\dot{Q}_{abs}} = \frac{\dot{Q}_{abs} - \dot{Q}_{th-loss}}{\dot{Q}_{abs}} \tag{4}$$

Unlike a conventional receiver in which instantaneous heat rate can be measured in terms of heat transfer fluid thermal capacitance rate and temperature rise, we can infer the net rate of heat capture by the CSPonD receiver only by measuring rate of salt mass temperature change (5a) approximated over discrete times steps by (5b):

$$\dot{Q} = -Mc_p\frac{d\overline{T}}{dt} \tag{5a}$$

$$\dot{Q}(t)\Delta t = -Mc_p\left(\widehat{\overline{T}}(t) - \widehat{\overline{T}}(t-\Delta t)\right) \tag{5b}$$

This procedure is used to measure $\dot{Q}_{th-loss}$ with $\dot{Q}_i = 0$ (heliostats unfocused) and $\dot{Q}_{stored}$with heliostats focused. The loss model obtained with aperture uncovered together with $\dot{Q}_{stored}$ permit us to measure $\dot{Q}_{abs}$.

Combining optical and thermal losses gives receiver overall efficiency:

$$\eta_{rcvr} = \frac{\eta_{opt}Q_i - Q_{th-loss}}{Q_i} = \eta_{opt}\eta_{th} \tag{6}$$

- *Design-Point efficiency*

In reporting results of on-sun testing under a small beam-down optics research pilot plant, we are faced with questions of how to translate those results to a bankable commercial design and scale. Because the aperture thermal losses at receiver operating temperature are essentially constant, receiver thermal efficiency varies mainly with incident flux density.

The Masdar Beam-Down Tower was built with an incompletely-populated heliostat field and a design concentration far below what can (and would have to) be achieved in a commercial beam-down plant. A build-out of the pilot plant is therefore proposed in Suppl. Note 1, section 6 to bring diameter-to-height ratio closer to (but still conservatively short of) commercial practice, i.e. from D/H = 1.95 to D/H = 3.49. The two adjustment factors needed to estimate design-point thermal efficiency correspond to the adjustments for DNI and solar field conditions (e.g. off-line heliostats) stipulated by the National Renewable Energy Laboratory (NREL) for power tower system performance tests (Kearney, 2013). The DNI factor is the ratio of design DNI to test DNI:

$$\gamma_{DNI} = \frac{DNI''}{DNI'} \tag{7}$$

The heliostat field factor is the ratio of zenith-projected built-out area ($''$) to test area ($'$) given approximately by:

$$\gamma_{built-out} = \frac{\sum_{\alpha=A}^{F} N_\alpha'' A_\alpha \cos\left(\frac{1}{2}\theta_\alpha\right)\rho_\alpha''}{\sum_{\alpha=A}^{C} N_\alpha' A_\alpha \cos\left(\frac{1}{2}\theta_\alpha\right)\rho_\alpha'} \tag{8}$$

where N_α is the number of on-line heliostats of area A_α in ring α and θ_α is elevation of central rays reflected from ring α. Note that (8) is not generally valid because it does not account for the unique projections of the sun on each heliostat; the approximation is close when intercept and beam-attenuation factors across rings is small and sun is positioned near the zenith. At this site zenith angle is $<10°$ on 22 June near solar noon. Adjustment for degradation and changes in cleanliness factor can be made via facet reflectances, ρ.

The absorbed and incident radiation for evaluation of design point performance is related to the test values by:

$$\dot{Q}_{abs}'' = \dot{Q}_{abs} \cdot \gamma_{built-out} \cdot \gamma_{DNI} = \eta_{opt} \cdot Q_i \cdot \gamma_{built-out} \cdot \gamma_{DNI} \quad (9)$$

Finally we can use the adjusted value of absorbed solar flux, $\dot{Q}_{abs}'$, to estimate design point thermal efficiency according to: $\eta_{th}'' = \frac{\dot{Q}_{abs}' - \dot{Q}_{th-loss}'}{\dot{Q}_{abs}'}$.

3. Experimental results

Starting June 5, 2017, 3.8 tonnes of nitrate salts were gradually loaded into the tank (Methods, section 2) and melted in-situ using ~80% energy from solar heat, over 4 days (Methods, section 3) and thermally cycled during 27 non-consecutive days between 280 °C and over 500 °C in the course of three months' cumulative operation. Following that, the entire salt mass was left in the tank to completely freeze and was later re-melted in-situ by the beam-down concentrator flux. Three freezing/re-melting cycles were completed without salt leaks or any other damage that could be detected (Suppl. Note 5, section 4).

Of the many observations that can be reported after initial operation of the prototype receiver and TES system, thermal behaviour during charging is undoubtedly of foremost interest as reported in the following sections.

3.1. Operating mode 1: Charging of the hot region at constant temperature with gradually increasing volume

In charging mode 1, the hot-region volume (upper region) is gradually increased by controlled downward motion of the divider plate (DP) such that a constant temperature is maintained. The purpose of Mode 1 is to enable concurrent charging and steam turbine operation by controlling the rate of DP motion to maintain the hot region at design temperature. For proof of concept it is only necessary to show that a constant, uniform temperature can be maintained while charging under time-varying DNI.

Fig. 5 shows the thermal evolution of molten salt temperatures between 09:00 and 17:00 on June 22, 2017 during a charging cycle that raised the average temperature from 350 °C to 475 °C in 7 h (09:00 to 16:00). One objective of this experiment was to test whether the mixing plate (MP) is needed to obtain a homogenous hot-region temperature. During the first charging hours, the MP was only moved slowly downwards, following the DP, so that no significant mixing action was introduced. When undesirable hot-region stratification started to develop after 12:00 noon, the MP was moved up and down to induce a mixing action. The effectiveness of DP and MP actions to maintain a uniform hot-region temperature during mode-1 charging is discussed in greater detail below.

Initially the MP and DP were placed near the top of the tank at 155 cm and 135 cm respectively (top-of-plate positions measured from floor of tank as shown in Fig. S7 of Suppl. Note 2). The thermocouple at 165 cm (number 12) is initially used to control movements of the two plates. A heating rate of about 100 K/h (constant slope from 350 to 450 °C) is observed between 09:00 and 10:00. Once this thermocouple reaches the desired temperature (450 °C in this experiment) the DP and MP were lowered by 2 cm, always keeping 15 cm between them to prevent collisions and possible collateral damage to the thermocouple profile probes. As the DP moves down, 350 °C salt creeps up from the cold region to the hot region via the annular passage between the tank wall and the DP. The entering cold salt mixes with the warmer salt above the DP, resulting in the first small decrease in temperature on the red curve labelled "12 (top)" at 10:03 am. Then as the new exposed volume of salt is heated we see the hot region temperature rise again.

Once the control temperature reaches 450 °C, the DP and MP are again lowered by 2 cm. This process is repeated until the next thermocouple, located at 150 cm (number 11), is uncovered by the falling MP at which time its signal becomes the new state variable governing motion control. The curves labelled 12 (top), 11, 10, 9, and 8 show that, one by one, each thermocouple and its corresponding stratum reach the desired temperature as the DP and MP are lowered.

However, after 3 h of operation, shortly after 12:00 when the DP was positioned at 99 cm (MP at 119 cm), the upper portion of the hot molten salt region began to overheat with thermocouples 8 to 12 rising above the 450 °C set point, while the lower portion of the hot region (thermocouples 5, 6, and 7) was not being heated sufficiently to reach 450 °C. This observed stratification is partly due to lengthening of the absorption path through the salt volume (Tetreault-Friend et al., 2017; Drotning, 1977) and partly to particulates stirred up by DP and MP motions which increase the effective salt absorptance. The DP and MP were then moved down every 5 min regardless of temperature. Once the DP and

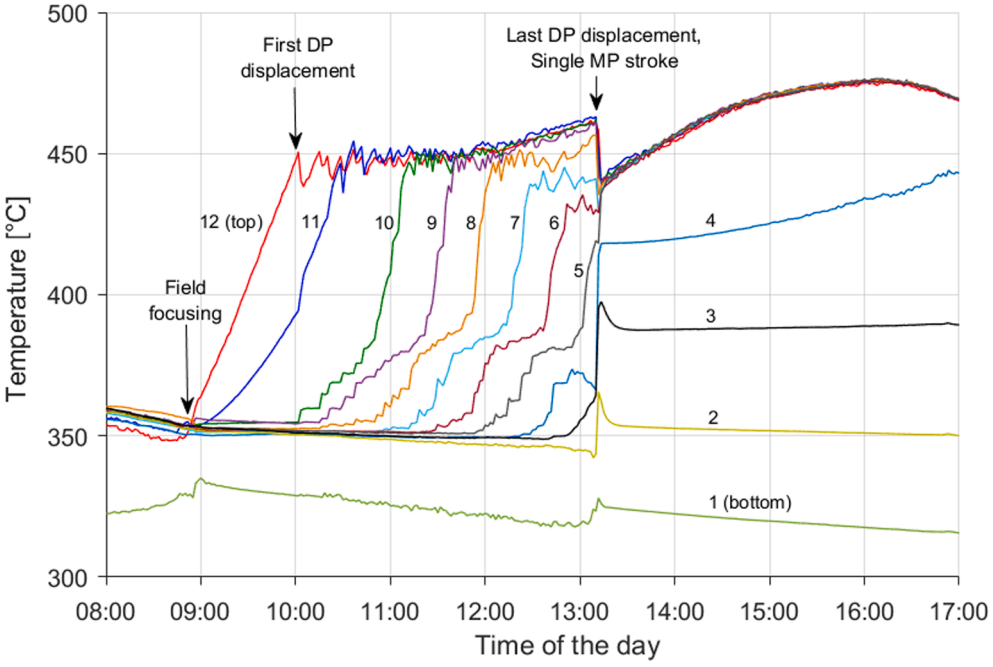

Fig. 5. Temperature profile in the molten salt for a charge between 350 °C and 475 °C on June 22, 2017. Each curve corresponds to the average temperature over a horizontal cross section at different depths as a function of time, where curve 1 (light green) corresponds to the bottom of the tank, and curve 12 (red) corresponds to the top. The height of the divider plate is progressively lowered to control the temperature of the hot salt layer. (For interpretation of the references to colour in this figure legend, the reader is referred to the web version of this article.)

MP reached their lowest position at 13:10 (DP at 60 cm and MP at 80 cm) the surface temperature was still above the set point. The MP alone was therefore moved rapidly through one up and down stroke at. 13:12 pm. This single mixing stroke resulted in nearly complete homogenization of temperature to around 440 °C. Subsequently all thermocouple readings, including tank wall temperatures, continued to rise in unison indicating that the amount of radiation reaching and absorbed by the tank walls is too small to result in local overheating. Heat charging of the salt is clearly dominated by volumetric absorption even at this small (sub-commercial) scale.

The salt temperature reached 475.3 ± 2 °C at 16:10 and the tank aperture was left open to observe tank thermal homogeneity with temperatures dropping thereafter under negative net flux (Fig. 7b).

Fig. 6 provides a different view of the June 22 thermal evolution, showing temperatures of the molten salt as a function of vertical position at 08:00 (the start of operation), before and after the up-down mixing stroke at 13:12, and at 16:00 (end of normal operation). At the beginning of the day, 08:00, the salt is uniform in temperature at about 350 °C. Right before the mixing stroke, 13:12, at 4.2 h into operation, the axial thermal profile ranges from about 350 °C to 460 °C while right after the up-down mixing stroke we see that the salt above the MP and DP assumes a uniform temperature of 440 °C. By the end of operation at 16:00, salt above the MP and DP has reached a uniform temperature of 475 °C.

The region below 70 cm corresponds to the tank volume occupied by the MP (5 cm thick) and the DP (30 cm thick), plus 15 cm clearance between the MP and DP, plus 20 cm dead volume occupied by non-participating salt below the DP to avoid restricting the cold region inlet. Because this non-participating volume is below the MP and beyond the reach of incident solar flux, it cannot be charged by volume absorption nor by convection from heated surfaces. However, the part of the salt between the MP and the DP was effectively charged by the mixing stroke.

By initiating a single mixing stroke, the tank surface temperature was reduced from 460 to 440 °C. After the mixing stroke, charging of the hot region continued to 475 °C while maintaining good thermal homogeneity.

Fig. 7a shows cumulative energy stored in the salt mass based on nine thermocouple profile probes with sensor depths T_1,…, T_{12}., for a total of 108 volumetrically distributed temperatures. At 08:00, the beginning of the day, uncovered tank thermal losses result in decreasing energy. When the solar field was focused at 08:45, tank stored energy began ramping up and maximum stored energy was achieved at 16:00.

Fig. 7b shows the instantaneous charge rate and DNI. The ratio of charge rate to DNI is highest near solar noon (12:20 UAE time at site longitude) when aggregate projected heliostat area is highest and off-axis aberration (Mokhtar et al., 2014; Kumar, 2015) is lowest. The ratio of charge rate to DNI is lower in the afternoon than in the morning because of increasing thermal losses from tank walls and aperture due to higher salt surface and vertical profile temperatures.

Between 12:00 and 13:00 the mean charging rate, $\dot{Q}_{stored}$, was found by (5b) to be 37.0 kW under mean DNI = 570 W/m^2 with mean salt surface temperature of 460 °C.

3.2. Operating mode 2: Charging of full tank with gradual temperature increase

If the CSP plant is to be used to generate electricity only after sunset, the temperature of the hot layer no longer needs to be maintained constant while charging. The receiver losses due to the exposed hot surface can be reduced by charging the entire volume uniformly from a colder state to a hotter state, rather than heating hot stratified layers at constant temperature from top to bottom. In this *fully-mixed, uniform charging mode* the DP and MP can be fixed (except for occasional MP mixing strokes if needed) at or near (depending on daily yield forecast) the bottom of the tank so that the fixed upper-region volume of salt is exposed to concentrated flux over the whole day. Fig. 8 shows the evolution of salt temperatures observed in charging mode 1 December 21, 2017. The five temperatures measured in the 70 cm deep region above the MP rise in nearly perfect unison.

In this case, the top of the DP and MP were fixed at 80 cm and 100 cm from the bottom of the tank, respectively. Temperature measurement

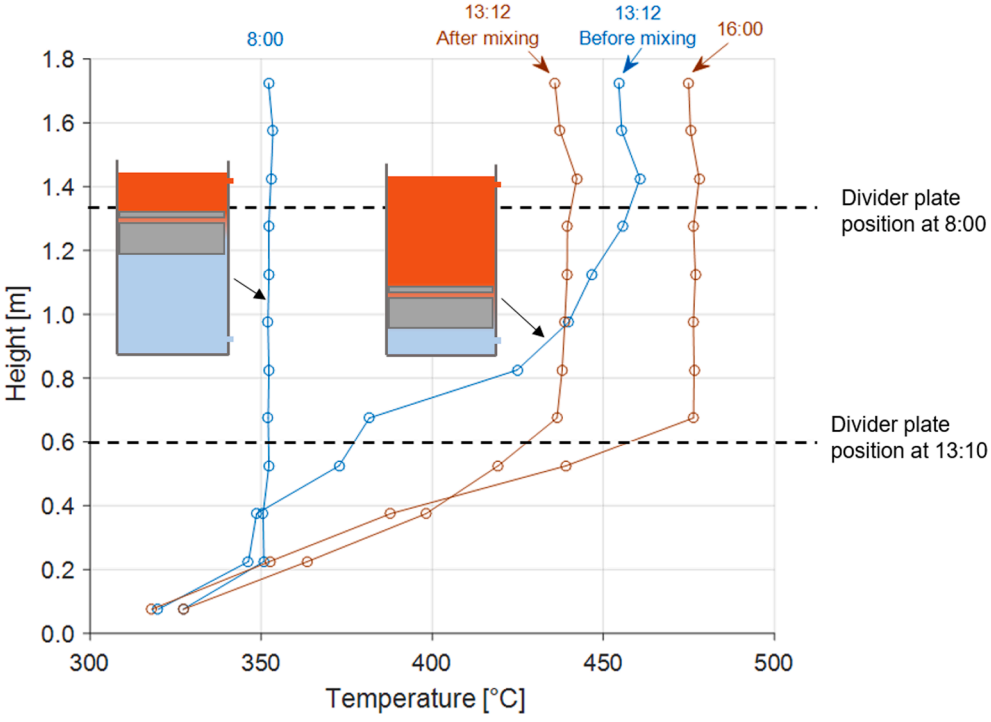

Fig. 6. Average temperature distribution in the molten salt at different times of the day for the same experiment on June 22, 2017. At 8:00, the DP and MP are located near the top of the tank. On and after 13:10, they are located at the bottom of the tank.

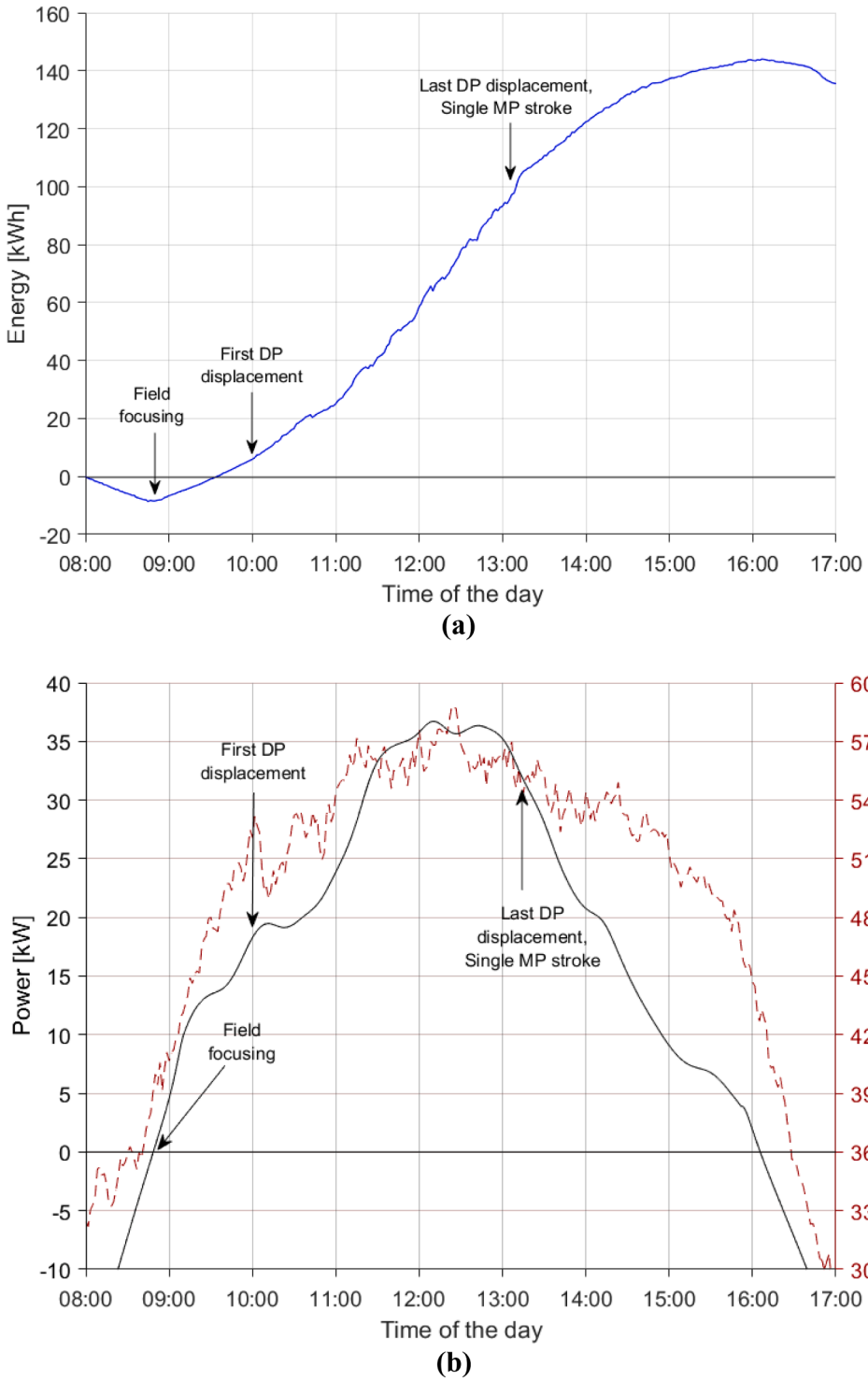

Fig. 7. (a) Cumulative energy stored and (b) Rate of energy stored in the molten salt tank versus time of the day from the same experiment on 22 June 2017.

levels 1 to 6 are located below the DP, level 7 is located between the MP and DP, and levels 8–12 are located in the useful volume of salt above the MP. Even with no MP motion, the vertical gradient of temperature in the useful volume of salt never exceeds 10 K/m. These results suggest natural convection from heating of the MP top surface is sufficient to passively mix the salts and maintain temperature uniformity throughout the heating process, despite the presence of any non-uniform volumetric solar absorption. Note however that stratification, needed during overnight discharge, will still be maintained by divider plate control regardless of the charging mode.

3.3. Receiver performance

The CSPonD receiver's performance may be expressed by two metrics, optical efficiency and thermal efficiency, or their product overall efficiency, using the analysis and assumptions presented in Methods, Section 2.4.

Optical Performance. The receiver's optical efficiency is defined (3) as the ratio of the solar flux absorbed by the salt and the receiver's inner surfaces to the total concentrated solar flux incident on the tank inlet aperture. The difference between these two quantities is the fraction of

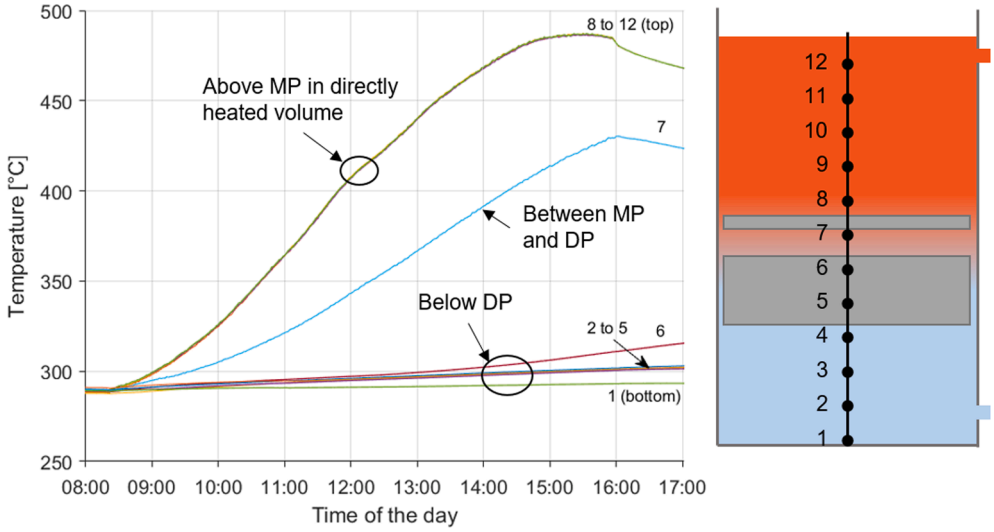

Fig. 8. Temperature profile in the molten salt during a charge from 290 °C to 487 °C with the DP fixed at 80 cm and MP at 100 cm on December 21, 2017. The useful volume of salt remains well mixed and highly uniform in temperature throughout the heating process. Temperatures profiles correspond to the average measured temperature at each level.

incident solar flux rejected by reflection from the salt surface and, to lesser extent, back through the aperture surface after one or more reflections from cavity walls.

For the present FOE geometry and plant configuration, receiver optical loss was found by ray-tracing and Fresnel equations to be about 3.8%, $\dot{Q}_{reject} \sim 0.038\dot{Q}_i$, varying only slightly with sun position (Kumar, 2015). The modeled receiver optical efficiency is therefore $\eta_{opt} \sim 96.2\%$ for the present configuration.

Recent characterization of nitrate salt optical properties suggests that at practical implementation scales, absorption over typical receiver path lengths (Fig. 8, Tetreault-Friend et al., 2017) will result in effective broadband absorption >0.95 within the MS volume even before encountering the mixing plate or interior wall surfaces. The small deviation from monochromatic behavior is discussed in supplementary note N5.2. Of the remaining 0.05 much will be absorbed on that first encounter and >0.95 will be absorbed by rays that return directly to the aperture after first (top of salt) reflection. Although absorption with in the salt volume is not entirely uniform (hence need for the mixing plate) it is clear that volumetric absorption is the primary mechanism by which the TES medium is heated. The CSPonD receiver does not employ an aperture window. Thus, first-surface reflection is the dominant and only significant optical loss.

Thermal Performance. The receiver's thermal efficiency is defined (4) as the ratio of the net rate at which heat is stored in the salt to the solar flux absorbed by the salt and the receiver's inner surfaces. The rate of thermal losses was evaluated from measurements of June 21st 2017 (Suppl. Note 2, section 6), and the net rate of heat stored in the salt was evaluated from measurements of June 22nd (Figs. 5–7). The sum of these two quantities provides the solar flux absorbed by the salt and receiver interior surfaces (rate of absorbed heat).

The experimental values of absorbed solar flux, $\dot{Q}_{abs} = 55.7$ kW and net rate of charge, $\dot{Q}_{abs} - \dot{Q}_{th-loss} = 37.0$ kW, provide an estimate of thermal efficiency under the low DNI test condition of 570 W/m^2 and existing limited heliostat field according to (4):

$$\eta_{th} = \frac{\dot{Q}_{abs} - \dot{Q}_{th-loss}}{\dot{Q}_{abs}} = \frac{37.0}{55.7} = 66.4\%$$

and an estimate of overall receiver efficiency by (6) of $\eta_{rcvr} = 63.9\%$. The experimental results can be translated to design point performance using the adjustments for DNI and solar field conditions stipulated by NREL for power tower systems performance tests (Kearney, 2013).

After adjustment for beam-down tower build-out and design point DNI of 900 W/m^2, an average flux density of 542 kW/m^2 is obtained at optical concentration ratio of 602 by a more fully-populated (but still conservative) heliostat field that could be practically realized at the Masdar beam down tower.. This provides a concentration approaching that of commercial plants but still not fully representative of the higher concentrations expected in an optimized scaled-up beam-down optical system (see Suppl. Note 1, section 6). Stipulated adjustments, the design-point receiver thermal efficiencies extrapolated from observed performance with the existing heliostat field, are $\eta_{th} = 93.4\%$ and $\eta_{th} = 91.5\%$ for salt surface temperatures of 500 and 550 °C respectively.

Multiplying the receiver's thermal and optical efficiencies according to (6), we obtain total receiver efficiencies $\eta_{rcvr} = 89.9\%$ and $\eta_{rcvr} = 88.0\%$ for salt surface temperatures of 500 and 550 °C respectively. These values are similar to the efficiencies reported by Ho and Iverson (2014) for high-temperature central receivers under a field concentration of 600.

4. Conclusion

3.8 tonnes of nitrate salts were melted in-situ with over 80% of the melting energy delivered by a 280 m^2 solar field over a period of four days. The molten salt was thermally cycled during 27 non-consecutive days between 280 °C and over 500 °C in the course of three months' cumulative operation. Following that, the entire contained salt mass was left to completely freeze and was re-melted in-situ. Three complete freezing and on-sun re-melting cycles were tested without any discernable damage or unexpected thermo-fluid behaviours. Movement of the DP and MP based on simple feedback control has maintained the desired vertical temperature profiles during charging. Through this extensive research/pilot scale on-sun testing we have demonstrated the feasibility of an open-top molten salt TES receiver with respect to the following criteria: (1) volumetric absorption performance, (2) thermal losses from the TES container and its entrance aperture, (3) salt absorptivity and degradation, (4) single-tank thermocline storage behaviour with moving divider plate and mixing plate, (5) simplicity of daily start-up and shut down, (6) robustness to occurrence of freezing/re-melting events (7) effectiveness of FOE dry-cooling system. Observations and analysis to date indicate that the molten salt direct absorption receiver is viable in all important respects.

The CSPonD receiver, achieved 64% overall efficiency with the existing limited (C = 145) heliostat field. Increasing D/H from 2.0 to 3.5

will lead to an 88% efficiency at DNI = 900 W/m^2, similar to that reported for power tower central receivers. At the same time, the single-tank receiver-TES provides several cost and operational advantages compared to conventional (tower receiver with 2-tank TES) power tower plants:

- Elimination of high-pressure pumps for cold-salt transport to the tower receiver, and of associated high parasitic energy consumption
- Reduced need or complete elimination of heat tracing for tower and receiver piping
- Initial melting of salt accomplished in-situ mainly by solar heat
- No need to drain the solar receiver at the end of each day's operation
- Reduced susceptibility to thermal shocks when focusing/defocusing or when clouds pass
- Reduced component cost by combining receiver and storage in a single tank, a cost advantage that is likely to grow as receiver and TES temperatures increase with transition to chloride salts.

Lessons learned include: 1) the mixing plate obstructs/reduces light penetration depth and may not be needed to prevent axial temperature gradients from developing in the hot region; 2) the divider plate is effective in blocking radiation from reaching the cold region, but, with current design, heat transfer between hot and cold regions is not substantially reduced over long time scales; 3) hoist tension sensors and variable speed winches are needed to improve plate movement control; 4) special attention is needed to protect mechanisms and instrumentation exposed to a dusty desert marine environment;

Future work should address:

- Continued operation of the 3.8-tonne prototype to assess reliability and obtain long term data on the durability of its materials—particularly stability of the exposed salt mass
- Improving automatic control of the divider plate to maintain homogeneous hot- and cold-region temperatures by smooth, continuous motions that track charge and discharge rates
- Enhancing passive mixing in the salt using radiation and natural convection modes to reduce or eliminate the need for active mixing
- Installing a low-head salt pump in the heat exchanger unit to test active discharging cycles, with a back-washable filter to remove solid particulates from the molten salt
- Improving the design of the DP to reduce conduction losses from the hot region to the cold
- Integrating an insulating solar-transparent cover to reduce thermal losses and salt evaporation. A cover consisting of floating hollow fused silica spheres that reduces losses up to 50% has already been demonstrated at lab-scale (Tetreault-Friend et al., 2018)
- Improving tank insulation to reduce the observed advection losses of porous insulation situated behind the molten salt tank's external cladding (Suppl. Note 2, section 6.2)
- Deploying the concept in a solar field configurations that provides higher concentrations
- Performing a techno-economic analysis of a full plant at commercial scale, with different configurations of multi-tower system (i.e. distributed steam generators with each solar-field/CSPonD unit and transport of steam to a central turbine, or central steam generator unit with transport of salt from the CSPonD units)

Results of The foregoing proposed efforts will facilitate testing at higher temperatures (565 °C and possibly up to 750 °C using chloride salts) with high thermal and thermodynamic efficiencies. Continued improvements in CSP receiver, FOE, and storage systems such as this will lead to truly cost-effective dispatchable solar power.

Author contributions

N. C. led the proposal and obtained the project grant, was Principal Investigator (PI) at Masdar Institute, participated to on-sun tests, drafted the article, and contributed to and edited the final manuscript.

A. H. S. was PI at Massachusetts Institute of Technology (MIT), participated in the first on-sun tests, drafted the article and contributed to the final manuscript.

A. G. was Post-Doctoral researcher on the design and construction of the pilot, prepared and directed initial on-sun tests, and contributed to the final manuscript.

B. G. was Post-Doctoral researcher on the design and construction of the pilot, contributed to the final manuscript.

R. L. was a PhD student working on the Final Optical Element (thermal management and optical integrity) as part of her thesis work, prepared and participated in on-sun tests, contributed to and edited the final manuscript.

T. T. H. developed the design and control of the mixing and divider plate, contributed to the final manuscript.

M. D. was a PhD student working on system optics as part of his thesis work, participated to first on-sun tests, contributed to and edited the final manuscript.

M. T. F. was a PhD student working on salt optical properties and tank thermal modelling as part of her thesis work and contributed to the final manuscript.

D. S. C. was consulting on prototype design and construction, designed and built the salt-to-air heat exchanger, and participated to first on-sun tests and contributed to the final manuscript.

D. L. T. was project co-PI at MIT, developed the design and control of the mixing and divider plate, supervised T. T. H.'s work.

P. R. A. initiated project discussions with MIT-CSPonD in 2010, was project co-PI at Masdar Institute, supervised optical modelling, optical alignment and flux measurement prior to on-sun test, supervised R. L. and M. D., participated to on-sun tests, contributed to and edited drafts and final manuscript.

Declaration of Competing Interest

The authors declare that they have no known competing financial interests or personal relationships that could have appeared to influence the work reported in this paper.

Acknowledgments

In memory of Dr. Thomas McKrell (1969-2017), a pioneer of the CSPonD.

This work is funded by the Masdar Institute/MIT collaborative flagship project, grant # FR2014-000002.

Masdar Institute and MIT acknowledge in alphabetic order: National Instruments and Parker/Sunpower.ae for donating part of instrumentation, control and motion systems, and SQM for kindly providing the nitrate salts for the pilot plant.

The authors would like to thank Víctor G. Pérez, David Díez Corral, and Djawed Belasri, research engineers at Masdar Institute, for their technical help and participation in building and operating the pilot plant, Vikas K. Kumar, Muna Al Qaydi, Juliana B. Torres, Akmal Khusanov and Lei Zhou, students at Masdar Institute and MIT for early work on the project, Guillermo Vázquez for technical discussions, and Mike Tiner, Director of Laboratories at Masdar Institute, for his constant support at the Solar Platform.

Finally, we thank the reviewers whose helpful and probing comments improved the paper substantially.

Appendix A. Supplementary material

Supplementary data to this article can be found online at https://doi.org/10.1016/j.solener.2021.02.058.

References

AlQaydi, M.S., Delclos, T., AlMheiri, S., McKrell, T., Calvet, N., 2016. Effect of sand and moisture on molten salt properties for open direct absorption solar receiver/storage system. AIP Conf. Proc. 1734, 050002.

Anonymous, 2018, Personal communication with an expert from a CSP EPC company, 2018.

Baum, V.A., Aparasi, R.R., Garf, B.A., 1957. High power solar installations. Sol. Energy 1.

Bohn, M.S., Green, H.J., 1989. Heat transfer in molten salt direct absorption receivers. Sol. Energy 42, 57–66.

Calvet, N., Martins, M., Grange, B., Perez, V.G., Belasri, D., Ali, M.T., et al., 2016. The Masdar Institute solar platform: A new research facility in the UAE for development of CSP components and thermal energy storage systems. AIP Conf. Proc. 1734, 100003.

Codd, D.S., 2011. Concentrated solar power on demand, PhD., Dept. of Mechanical Engineering, Massachusetts Institute of Technology (MIT), Cambridge, MA.

Delameter, W.R., Bergan, N.E., 1986. Review of the Molten Salt Electric Experiment, Sandia National Laboratories.

Diago, M., Crespo Iniesta, A., Soum-Glaude, A., Calvet, N., 2018a. Characterization of desert sand to be used as a high temperature thermal energy storage medium in particle solar receiver technology. Appl. Energy 216, 402–413.

Diago, M., Calvet, N., Armstrong, P.R., 2020. Net Power Maximization in a Faceted Beam-down Solar Concentrator. Sol. Energy 204 (1), 476–488.

Diago, M., Armstrong, P.R., Slocum, A.H., Calvet, N., 2018b. Where should beam down heliostat central rays intersect the final optical element axis? In: AIP Conference Proceeding - SolarPACES 2017 conference, Chile, vol. 00.

Drotning, W.D., 1977. Optical properties of a solar-absorbing molten salt heat transfer fluid. Sandia National Laboratories.

Drouot, L.P., Hillairet, M.J., 1984. The Themis Program and the 2500-KW Themis Solar Power Station at Targasonne. J. Sol. Energy Eng. 106, 83–89.

Epstein, M., Segal, A., Yogev, A., 1999. A molten salt system with a ground base-integrated solar receiver storage tank. J. Phys. IV France 09. Pr3-95-Pr3-104.

Gil, A., Codd, D.S., Zhou, L., Trumper, D., Calvet, N., Slocum, A.H., 2016. Concentrated solar power on demand demonstration: Construction and operation of a 25 kW prototype. AIP Conf. Proc. 1734, 050017.

Gil, A., Codd, D.S., Zhou, L., Trumper, D., Campbell, R.B., Grange, B., et al., 2015. Design of a 100 kW Concentrated Solar Power on Demand Volumetric Receiver With Integral Thermal Energy Storage Prototype. In: Proc. ASME: POWER2015-49504, San Diego, USA.

Grange, B., Kumar, V., Gil, A., Armstrong, P.R., Codd, D.S., Slocum, A., et al., 2015. Preliminary Optical, Thermal and Structural Design of a 100 kWth CSPonD Beam-down On-sun Demonstration Plant. Energy Procedia 75, 2163–2168.

Hamer, T.T., Zhou, L., Trumper, D.L., Slocum, A.H., Calvet, N., 2017. An Origami-Inspired Design of a Thermal Mixing Element Within a Concentrated Solar Power System, p. V05BT08A061.

Hamer, T.T., Zhou, L., Trumper, D., Slocum, A.H., Calvet, N., 2017b. Implementation of Thermal-Insulating and-Mixing Elements in a Concentrated Solar Power on Demand System. In: AIP Conference Proceeding - SolarPACES 2017 conference, Chile, vol. 00.

Hasuike, H., Yuasa, M., Wada, H., Ezawa, K., Oku, K., Kawaguchi, T., Mori, N., Hamakawa, W., Kaneko, H., Tamaura, Y., 2009. Demonstration of Tokyo Tech Beam-Down Solar Concentration Power System in 100kW Pilot Plant. Presented at the SolarPACES 2009, Berlin, Germany.

Hildebrandt, A.F., Vant-Hull, L.L., 1975. A Tower-Top Point Focus Solar Energy Collector. In: Veziroğlu, T.N. (Ed.), Hydrogen Energy. Springer, Boston, MA.

Ho, C.K., 2017. Advances in central receivers for concentrating solar applications. Sol. Energy 152, 38–56.

Ho, C.K., Iverson, B.D., 2014. Review of high-temperature central receiver designs for concentrating solar power. Renew. Sustain. Energy Rev. 29, 835–846.

Iniesta, A.C., Diago, M., Delclos, T., Falcoz, Q., Shamim, T., Calvet, N., 2015. Gravity-fed combined solar receiver/storage system using sand particles as heat collector, heat transfer and thermal energy storage media. Energy Procedia 69, 802–811.

Kearney, D., 2013. Utility-Scale Power Tower Solar Systems: Performance Acceptance Test Guidelines. National Renewable Energy Laboratory NREL, Golden, CO, Subcontract report.

Kumar, V., 2015. Modeling of Beam Down solar Concentrator and Final Optical Element Design, MSc. thesis, Masdar Institute, Abu Dhabi.

Lahlou, R., Armstrong, P., Grange, B., Almheiri, S., Calvet, N., Slocum, A., et al., 2016. Thermal modeling of a secondary concentrator integrated with an open direct-absorption molten-salt volumetric receiver in a beam-down tower system. AIP Conf. Proc. 1734, 020012.

Lahlou, R., Armstrong, P.R., Calvet, N., Slocum, A.H., Shamim, T., 2018. Testing of a Secondary Concentrator Integrated with a Beam-Down Tower System under Non-liquid Cooling Strategies. In: AIP Conference Proceeding - SolarPACES 2017 Conference, Chile, vol. 00, p. 00000.

Lilliestam, J., Labordena, M., Patt, A., Pfenninger, S., 2017. Empirically observed learning rates for concentrating solar power and their responses to regime change. Nature Energy 2, 17094.

Mark Mehos, Hank Price, Robert Cable, David Kearney, Bruce Kelly, Gregory Kolb, Frederick Morse: Concentrating Solar Power Best Practices Study, NREL/TP-5500-75763, June 2020.

Meyers, S.A., 2011. Thermal and Optical Characterization of the Beam Down Solar Thermal Concentrator at Masdar, MSc. thesis, Masdar Institute, Abu Dhabi.

Mokhtar, M., Meyers, S.A., Armstrong, P.R., Chiesa, M., 2014. Performance of a 100 kWth Concentrated Solar Beam-Down Optical Experiment. J. Sol. Energy Eng. 136, 041007.

Passerini, S., 2010. Optical and chemical properties of molten salt mixtures for use in high temperatures power systems, M.Sc., Dept. of Nuclear Science and Engineering, Massachusetts Institute of Technology (MIT), Cambridge, MA.

Pitz-Paal, R., 2017. Concentrating solar power: Still small but learning fast. Nature Energy 2, 17095.

Reilly, H.E., Kolb, G.J., 2001. An Evaluation of Molten Salt Power Towers Including Results of the Solar Two Project. Sandia National Labs, Albuquerque, NM ; Livermore, CA, 2001.

Singer, C., Buck, R., Pitz-Paal, R., Müller-Steinhagen, H., 2013. Economic chances and technical risks of the internal direct absorption receiver. J. Sol. Energy Eng. 136, 021013–021013-11.

Skinrood, A.C., Brumleve, T.D., Schafer, C.T., Yokomizo, C.T., Leonard, C.M., 1974. Status Report of a High Temperature Solar Energy System, SAND74-8017.

Slocum, A.H., Codd, D.S., Buongiorno, J., Forsberg, C., McKrell, T., Nave, J.-C., et al., 2011. Concentrated solar power on demand. Sol. Energy 85, 1519–1529.

SolarPACES. (October 2020). CSP Projects Around the World. Available: http://www.solarpaces.org/csp-technology/csp-projects-around-the-world.

Speidel, P.J., Kelly, B.D., Prairie, M.R., Pacheco, J.E., Gilbert, R.L., Reilly, H.E., 1999. Performance of the solar two central receiver power plant. J. Phys. IV France 09. Pr3-181-Pr3-187.

Tabor, H., 1981. Review Article: Solar Ponds. Solar Energy 27 (4), 181–194.

Tetreault-Friend, M., Gray, L.A., Berdibek, S., McKrell, T., Slocum, A.H., 2017. Optical properties of high temperature molten salt mixtures for volumetrically absorbing solar thermal receiver applications. Sol. Energy 153, 238–248.

Tetreault-Friend, M., Diago, M., Cooper, T.A., Gray, L.A., Slocum, A.H., 2018. A floating modular cover for high temperature open-tank molten salt solar-thermal volumetric receivers. Sol. Energy 176, 465–482.

US DOE Office of Energy Efficiency & Renewable Energy. (October 2017). Concentrating Solar Power. Available: https://energy.gov/eere/solar/concentrating-solar-power.

Vazquez, 2017, Personal communication with G. Vazquez, CSP expert at Masdar Clean Energy.

Viskanta, R., 1987. Direct Absorption Solar Radiation Collection Systems. In: Yüncü, H., Paykoc, E., Yener, Y. (Eds.), Solar Energy Utilization vol. 129, Springer, Dordrecht, pp. 334–360.

West, R.E., 1987. Direct Absorption Receiver system for High Temperature. In: Yüncü, H., Paykoc, E., Yener, Y. (Eds.), Solar Energy Utilization, Springer, Dordrecht, pp. 361–373.